Master Thesis

Author:
Erik Kool

A systematic search for near-infrared counterparts to ultraluminous X-ray sources

Institute:
Netherlands Institute for Space Research (SRON)
Utrecht University

Supervisors:
Peter Jonker
Manuel Torres

August 25, 2012

Abstract

The nature of ultraluminous X-ray sources (ULXs) remains unclear as it is still not understood whether they contain stellar mass black holes or intermediate-mass black holes (IMBHs). As a first step to answer this question we report a systematic search for near-infrared counterparts to ULXs. We observed 23 ULX X-ray positions, typically accurate to $\lesssim 1''$, in host galaxies <10 Mpc in the K_s-band with LIRIS at the WHT on La Palma. The data reduction, astrometry and the coaddition of the images was performed with data reduction package THELI. Relative photometry with respect to 2MASS stars produced apparent magnitudes of the detections and limits on the depth of the images. We found 6 detections within the error circle of the ULX X-ray positions. Based on chance alignment calculations we conclude that all detections are very likely associated with the ULX detections in X-ray. We measured apparent magnitudes in K_s of the detections of 15.8 to 20.0. The corresponding absolute magnitudes ranged from -8.1 to -14.2, which are suggestive of red supergiants with the exception of the brightest detection, at X-ray position X-2 in NGC 2500. This extended source is most likely a foreground source or star cluster. These detections represent the first identifications of near-IR counterparts to ULXs to date. The brightest counterparts found are primary candidates for spectroscopy to unambiguously identify the donor star, and ultimately time-resolved photometric and spectroscopic observations to obtain a mass-limit to the black hole in the ULX.

Contents

Chapter 1

Introduction

1.1 Definition of an ultra-luminous X-ray source

In 1978 the first fully imaging X-ray telescope *Einstein Observatory* was put into space, after which a number of non-nuclear and extremely luminous X-ray sources in nearby galaxies were found. Later X-ray satellites with greater spectral and angular resolution (for example *ROSAT* and more recently *XMM-Newton* and *Chandra*) confirmed that these were indeed single and very luminous X-ray sources, and not blends in crowded fields or transient events. These ultra-luminous X-ray sources (ULXs) have luminosities from $\sim 10^{39}$ up to $\sim 10^{41}$ erg s^{-1} and are commonly assumed to be non-nuclear accreting black holes. Fig. 1.1 gives an artist impression of an accreting black hole[1]. For an X-ray source to be defined as a ULX it has to be observed at least once with a peak luminosity above the Eddington limit of a 10 $M_\odot$ stellar mass black hole (sMBH), assuming isotropic radiation. The Eddington luminosity is the maximum radiative luminosity of an accreting compact object. This is the luminosity where the radiation force outwards is balanced by the gravitational force inwards in hydrostatic equilibrium. Beyond the Eddington luminosity, stable isotropic accretion is no longer possible since the radiation pressure would drive off any material from the star. For spherical accretion of fully ionized hydrogen the Eddington limit is approximately:

$$L_{edd} \approx 1.3 \cdot 10^{38} \frac{M}{M_\odot} \text{ erg s}^{-1} \tag{1.1}$$

where M is the black hole mass [1].
Galactic black hole binaries generally contain a stellar black hole with a mass of ≈5-15 $M_\odot$. This means the upper limit on its luminosity, the Eddington luminosity, for an sMBH is $\sim 10^{39}$ erg s^{-1}. Therefore it is generally accepted that ULXs have peak luminosities of $L_x > 10^{39}$ erg s^{-1}.
There are several scenarios that try to explain these high accretion luminosities. The straightforward explanation is that the black hole of the system is more massive than an sMBH. Since the Eddington limit is proportional to the black hole mass, the luminosity of a ULX would fall well within the Eddington limit for a more massive black hole of 10^2-10^4 $M_\odot$. However, this would represent a class of so far unobserved black holes, with masses between stellar black holes and supermassive black holes in AGN. Another explanation is that the radiation pattern is highly anisotropic, so that the high apparent brightness is due to beamed emission in our line of sight, either due to strong relativistic beaming or mild geometrical beaming in combination with super-Eddington accretion. The latter means that the accretion rate of the binary system is high enough for the source to exceed the Eddington limit. In the next section the advantages and problems with these scenarios are discussed, beginning with beamed emission and super-Eddington accretion.

[1]By Rob Hynes, see http://www.phys.lsu.edu/∼rih/binsim/.

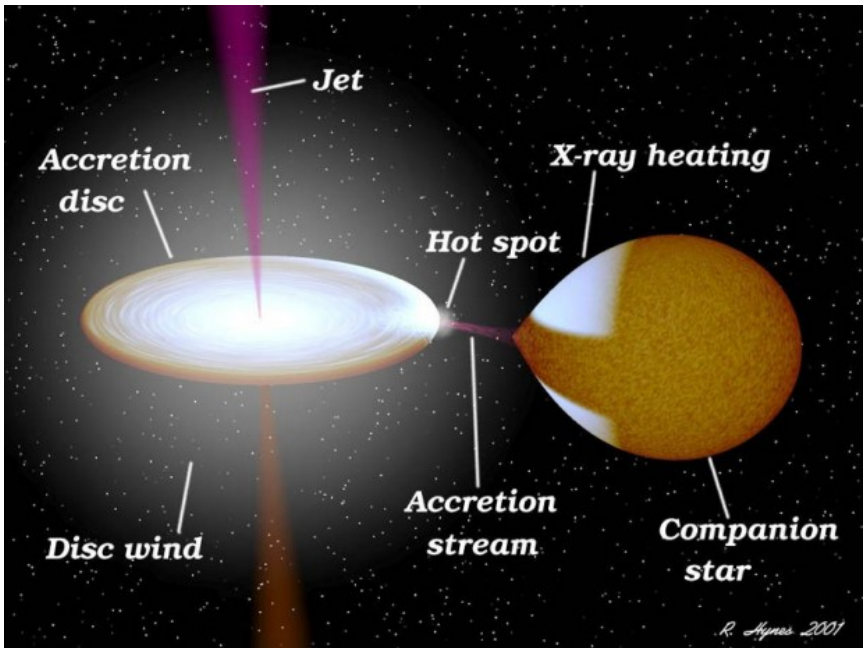

Figure 1.1: Artist impression of an X-ray binary by Rob Hynes, with the main components of a binary system as indicated. It is not to scale, since a ULX most likely contains a much more massive (super)giant as companion star.

1.1.1 Beaming and super-Eddington accretion

Relativistic beaming is the process by which the apparent luminosity of emitting matter is modified by relativistic effects. An accreting compact object can form two opposing relativistic jets of plasma that will cause a dramatic difference in emission depending on the angle in which the system is viewed. This beaming-scenario was proposed to explain the apparent high luminosities of ULXs [2], but soon ran into difficulties. It predicts that for every high luminosity source, there should be a large number of lower luminosity sources; around 30 sources of $L_x \sim 10^{39}$ erg s^{-1} for every source of $L_x \sim 10^{40}$ erg s^{-1}. However not more than $\approx$ 5-10 sources at 10^{39} erg s^{-1} are found relative to the number of sources with luminosity 10^{40} erg s^{-1}. Thus this scenario requires a large number of jet sources beamed in other directions, for which there is no observational evidence. Finally, compact objects that are the source for relativistic beaming often have a radio counterpart, but this is not the case for most observed ULXs.

While strong relativistic beaming is now ruled out as a viable explanation for ULXs, it is possible that mild geometric beaming is still an important contributer to the high luminosity of ULXs, in combination with super-Eddington accretion. The theory of super-Eddington black hole accretion was developed in the 1980s with the slim disk model [3]. Here narrow funnels along the rotation axis of the accretion disk collimate radiation into beams, resulting in an apparent high luminosity as a combination of collimation and super-Eddington accretion rates. Later simulations supported this idea and it was shown that even with a moderately super-critical mass supply an apparent luminosity $\approx 20\ L_{Edd}$ could be reached for face-on observers [4]. It has also been suggested that strong density inhomogeneities in the accretion disk could cause escaping flux to exceed the Eddington limit by a factor of $\sim 10 - 100$ [5].

The main advantage of this scenario is that ordinary stellar mass black holes can be sufficient for the system to reach the luminosity observed for most ULXs. These sMBHs have already been identified as the compact objects in Galactic X-ray binaries. Secondly, sMBHs are the easiest to form based on standard stellar models, as the final stage of the

evolution of a massive star. But despite everything this scenario dóes mean violating the Eddington limit and while models show that this is possible in theory, so far the Eddington limit works well for almost all known Galactic black holes, neutron stars and AGN. Also, the ULXs with the largest luminosities can still not be explained by use of an sMBH.

1.1.2 Intermediate Mass Black Holes

The last scenario consists of a system with a black hole more massive than a $\sim$10 $M_\odot$ sMBH. Since the Eddington limit depends on the mass of the accreting compact object, if the black hole of the binary system is massive enough the luminosity of a ULX does not have to exceed the Eddington limit. In current stellar evolution models the mass distribution of the black hole remnants of massive stars is peaked around 10 $M_\odot$, but has a tail up to $\lesssim 100\ M_\odot$. The mass of a compact object depends on the initial mass of the progenitor and how much mass is lost during the progenitors evolution. Mass is lost through stellar winds and strongly depends on the metallicity of the star. For a low metallicity star ($\sim$ 0.01 solar metallicity) it is possible to leave a black hole of $\lesssim 70 M_\odot$ [6]. Assuming such a black hole accretes at the Eddington limit, it is possible to explain ULXs up to a few $\times 10^{40}$ erg s^{-1}. To power such a luminosity a large mass reservoir is required, suggesting that these systems are high-mass X-ray binaries (HMXB). This possibility is further strengthened by the observation that most ULXs are spatially and temporally closely associated with star-forming regions. Since an HMXB usually consists of a compact object with a short-lived O or B star, they are oftentimes fonud in these regions.
Therefore a HMXB with a very massive sMBH, formed by a low metallicity progenitor, can explain most observed ULX luminosities. But this is based on the assumption that the ULX radiates at or very near the Eddington limit. However, most observed neutron stars and sMBH X-ray binaries have accretion rates smaller than the Eddington limit ($\sim$0.1 Eddington). To explain ULXs at these smaller accretion rates it is necessary for the ULX to have an even more massive black hole as the compact object, with a mass of $10^2\ M_\odot - 10^4\ M_\odot$. While stellar black holes up to $\sim 16 M_\odot$ (for example in M33 X-7 [7]) and supermassive black holes in AGN with masses of $> 10^5 M_\odot$ are identified, black holes with masses of several hundred to a few thousand solar masses remain elusive. These intermediate mass black holes (IMBHs) would be massive enough to be able to emit at ULX luminosities without exceeding the Eddington limit, but light enough not to sink to the center of their host galaxies by dynamical friction. It is not yet clear how an IMBH can be formed, since the core collapse of an isolated star will not create a massive enough black hole according to current stellar evolution models. In very massive stars ($\gtrsim\ 130 M_\odot$) production of free electrons and positrons, due to increased gamma ray production, reduce thermal pressure inside the core. This eventually leads to a runaway thermonuclear explosion that completely disrupts the star without leaving a black hole, causing the upper limit for a stellar black hole of $\sim\ 70 M_\odot$. It has been suggested that very early metal-free Population III stars could have had masses above this pair-instability limit and collapsed into IMBHs [8]. Another option for the creation of such a massive star is due to mergers and collisions in young and dense star clusters. Finally, an IMBH could be the result of high enough accretion by an sMBH to grow by a factor of ~ 100, or tidal stripping of satellite galaxies, exposing the nuclear black hole.
While all scenarios offer an explanation for ULXs, they also are accompanied by significant problems. A way to distinguish between the different scenarios would mean a major step forward in understanding the nature of ULXs.

1.2 Can one distinguish between the models?

If ULXs are IMBHs, it is of great interest how these are formed in comparison with stellar mass black holes. In case of super Eddington accretion rates, these objects are interesting for accretion theory. Either way, it is important to be able to distinguish between the several ULX scenarios. The main difference between these scenarios is the mass of the accreting black hole. If it is possible to obtain a reliable measurement of the black hole mass, it would shed light on the nature of ULXs. So far there have been many attempts made to provide an answer to this question. One approach is based on the knowledge of Galactic sMBH binaries, by comparing emission state properties. A second method is identifying the counterpart of the black hole, and by dynamical mass determinations obtain limits to the black hole mass. The properties of these methods are treated in the next section. For a detailed review of the history and current state of ULX research, see Feng and Soria [9].

1.3 Mass measurements

1.3.1 X-ray states and variability

Emission of black hole binaries has been classified into four states: quiescent, hard, thermal and steep-power law [10]. The thermal state is well explained by the standard accretion disk model, where the emergent X-ray spectrum is described by a multicolor disk that depends on the inner radius of the disk and the temperature at that radius [11]. In the thermal state this radius is assumed constant and the related innermost stable circular orbit depends on the mass and spin of the black hole. This state has been observed for many Galactic black hole binaries and shows distinctive properties, like a fourth-power dependence of the temperature on the bolometric disk luminosity, and a low level of short-term variability. If ULXs are found in this state, the mass and spin could be inferred from a Galactic black hole binary with the same properties. For a ULX in M82 this has been done, with a resulting mass between 200 $M_{\odot}$ and 800 $M_{\odot}$ [12]. In this case the spin of the black hole is assumed to be fast, to set a limit on the super-Eddington accretion rate. However, Okajima et al. [13] applied a super-Eddington slim-disk spectral model to the same source and found a mass of 19-32 $M_{\odot}$. This shows the problem with fitting masses based on spectral states, it is often based on fitting solutions that are not unique and uncertain for most sources. So far it has been proven difficult to provide an accurate prediction of the black hole mass of a binary based on the spectral state.
Another method of mass scaling is looking at the X-ray variability of a source. One aspect of this variability involves quasi-periodic oscillations (QPO). As the name suggests these variations in the arrival times of X-ray light occur at certain frequencies in a not quite but nearly periodic manner. sMBHs and AGN seem to be correlated based on black hole mass, accretion rate and the characteristic frequency that is related to these QPOs. For some ULXs it is suggested that the black hole mass can be found with this relation, using a certain type of QPOs that are detectable in ULXs [14]. The problem with this method is that for ULX observations the signal-to-noise ratio is not nearly as good as for Galactic black hole binaries, limiting the number of QPOs found. The QPOs that are found in ULXs are few, and it is not easy to conclude which QPO types from sMBH binaries they relate to.

1.3.2 Dynamical mass measurements

For sMBH binaries a tried and proven method in obtaining a mass measurement for the compact object is by using radial velocity curves and light curves. The light curve of a

system shows the light intensity as a function of time. For a binary system this can vary periodically due to various reasons. At the right inclination angle to our line of sight the sources move in front of each other, (partly) eclipsing the other. The light curve of such an eclipsing binary shows dips in the light intensity, which makes it possible to deduce

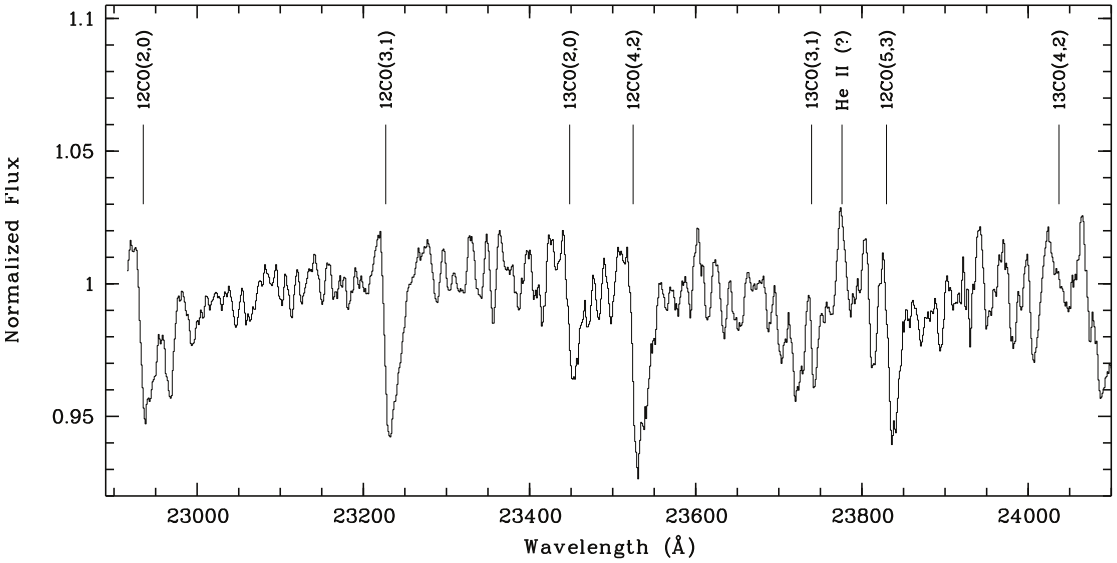

Figure 1.2: Observed K-band spectrum of X-ray binary GRS 1915+105 with clear spectral lines, obtained at the ESO VLTAntu telescope [15].

parameters of the system like the relative sizes of the two objects. It is also possible that the shape of the donor star is distorted due to the presence of the black hole, called ellipsoidal modulation. Given the high mass transfer rate in the case of ULXs this is likely to be the case. To explain the luminosity of a ULX the donor star must supply a high enough mass transfer rate and sustain this rate long enough to account for the number of ULXs observed. This high mass transfer rate can most easily be explained if the donor star fills its Roche lobe. This is the region of space around a star in a binary system within which orbiting material is gravitationally bound to that star. If the donor star fills this region, its shape will be distorted, see Fig. 1.1, and depending on which angle the star is viewed from, the light intensity will vary. From this ellipsoidal modulation the orbital period and possibly the inclination of the system can be extracted, in absence of eclipses. The estimation of the inclination is complicated by heating of the surface of the donor star that faces the compact object. Depending on the phase of the donor star in the line of sight, the intensity will change and so will the light curve.
A dynamical mass measurement also needs a radial velocity curve of the system, which is measured using periodically varying Doppler shifted spectral lines. An example of spectral lines in the K-band is shown in Fig. 1.2. The Doppler shift is caused by the movement of the objects of the binary around the center of mass of the system along the line of sight. If the radial velocity of the donor star is obtained, the half-amplitude K of this curve and the period found from the light curve or radial velocity measurements lead to the mass determination of the black hole. By combining Newton's law of gravitation and motion a quantity known as the mass function can be calculated:

$$f(M) : \frac{P}{2\pi G} K^3 = \frac{M_x^3 \sin^3 i}{(M_d + M_x)^2} = M_x \left(\frac{M_x}{M_d + M_x} \right)^2 \sin^3 i \tag{1.2}$$

Here M_d and M_x are the masses of the donor star and black hole respectively, P is the orbital period, G is Newton's gravitational constant and i the inclination of the system.

Knowledge of P and K alone gives a lower limit of the mass of the black hole M_x, since $\sin^3 i < 1$ and $(\frac{M_x}{M_d+M_x})^2 < 1$. If from the light curve the inclination can be obtained and from the broadening of the absorption lines the mass ratio $q = \frac{M_d}{M_x}$, from equation 1.2 the BH mass M_x can be derived. However, to derive the inclination of a ULX from the light curve will be difficult to accomplish because of the contribution of the disc to the light curve, which will diminish the signal[2]. Also, computing the mass ratio from broadened absorption lines is based on the assumption that the donor star is in forced corotation, an assumption that is doubtful for ULXs due to the limited lifetime of the donor star. This means that obtaining a mass limit for a ULX BH is possible, but a specific mass is not.
Since there are no ULXs in our own galaxy, the ULXs that we observe are at large distances. Therefore it is not trivial to measure the radial velocity curve from the counterpart of a ULX due to their faintness (in optical V$\geq$ 22 mag). And before a dynamical mass measurement can be attempted, first the counterpart must be identified. So far about 15 ULXs have been identified with a single or several counterparts. A few attempts have been made in determining the mass of the black holes by dynamical mass measurements. Because the optical light is dominated by the bright and varying disk the shallow narrow absorption lines of the donor star are not observable, and instead emission-lines were used, specifically He II λ4686. The results of these attempts were either inconclusive, [16] [17], or the lines varied randomly instead of showing orbital modulation [18].
A model constructed by Copperwheat et al. [19] suggests that observations in infrared will be more useful in determining the counterpart and further spectroscopy. This model assumes a binary system with a black hole accreting matter from a Roche Lobe filling companion star, taking into account effects of radiative transport and radiative equilibrium in the irradiated surfaces of both the star and a thin accretion disk. Fig. 1.3 shows the

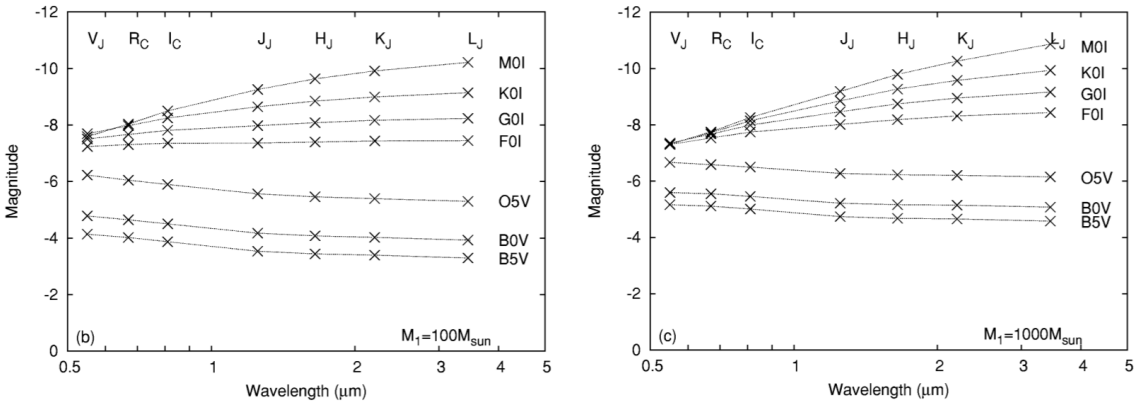

Figure 1.3: Absolute magnitudes of several stellar type stars and discs for BH masses of 100 $M_\odot$ (left) and 1000 $M_\odot$ (right) according to the model by Copperwheat et al. [19] at wavelengths 0.5-4.0 μm. X-ray luminosity is taken to be 10^{40} erg s^{-1}, $\cos i = 0.5$ and the star is at superior conjunction.

absolute magnitudes of stars and discs of several stellar types at wavelengths 0.5-4.0 μm for increasing BH masses, based on the model by Copperwheat et al. It shows that for high BH masses the absolute magnitude of an M- or K-supergiant is much brighter in infrared than any star/disc in optical. Assuming that at least a part of ULXs consist of a red supergiant and an IMBH, they will be more easily detectable in near-IR than ULXs that contain a blue supergiant are detectable in optical. Apart from that accretion discs are in general very bright in optical, which makes it difficult to distinguish the donor star in optical observations, while the contrast in near-IR between the disc and a bright red supergiant donor star might be much larger.

[2] An exception are transient discs, which can be in a very low luminosity quiescent state.

In summary, obtaining a reliable mass measurement of the black hole of a ULX would give a much better insight in the nature of these sources. Measuring the radial velocity curve and light curve of a ULX would provide such a reliable measurement, but due to the distance of known ULXs and the faintness of their counterparts this is not easy. Observations in optical wavebands of counterparts so far have not resulted in conclusive results. Based on the model by Copperwheat et al. [19] observations in infrared might have more diagnostic power in determining the characteristics of ULXs. It then makes sense to observe ULXs in infrared for counterparts and that way have a better chance of measuring absorption line Doppler shifts to obtain a radial velocity curve of the donor star. As can be seen in Fig. 1.2 clear absorption lines of an X-ray binary are detectable in the K-band. But first these infrared counterparts need to be identified. This is the first step in measuring the mass of potentially a new class of black holes, and the subject of this thesis. In the next chapter the method for identifying ULX counterparts is described, and in the following chapter the results are treated. Finally in the last chapter the results are discussed.

Chapter 2

Method

2.1 Observations

Identifying counterparts of ULXs is the first step in determining the mass of the black holes of ULXs. Ultimately the mass determination will be based on a spectrum with a high enough resolution to positively identify absorption lines. To make sure that observing such a spectrum of a counterpart is possible, the ULX should not be at too large a distance. Therefore we set a limit on the distance to the ULXs to be observed at ∼10 Mpc. At a distance of 3 Mpc a source with an absolute magnitude of -10.2, typical for an M-type supergiant, will have an apparent magnitude of ∼17.2. At a distance of 10 Mpc, the magnitude of such a source will be as faint as ∼19.5, which is at the limit of what can be observed with a ground-based spectrograph nowadays.

2.1.1 Instrument: LIRIS near-IR imager on the WHT

The images of the ULXs were obtained with LIRIS at the William Herschel Telescope (WHT). The WHT is a 4.2 m optical/near-infrared reflecting telescope located at the Observatorio del Roque de los Muchachos on the island of La Palma, Canary Islands. The telescope can be auto-guided during observations, where a guide star is hold at a certain position. This prevents the observed field and sources from drifting during long observations.
The instrument LIRIS (Long-slit Intermediate Resolution Infrared Spectrograph) uses a 1024×1024 HAWAII near-infrared detector, with a pixel scale of 0.25″/pixel, yielding a field of view of 4.27′×4.27′. The image mode of LIRIS was used with a K_s filter with an effective band from 1.99-2.31 μm.
An IR detector such as LIRIS consists of an array of pixels that convert incoming photons into electrons that are collected during an exposure. Full well is the maximum number of electrons that can be collected by a pixel before saturation. At readout the electrons are converted into a number that is called the count of the pixel, in terms of Analog-to-Digital Units (ADU). LIRIS is linear up to a count of 25 kADU (< 2% nonlinearity) and has a saturation limit at 45 kADU. The instrument has a readout noise of < 3 e^- and a gain of 3.5-3.7 e^-/ADU, the electron to ADU conversion rate.
As most near-IR detectors, LIRIS suffers from an effect called reset anomaly. When the detector is not observing it is continuously resetting, quickly reaching *resetting equilibrium*. During exposures it reaches an *imaging equilibrium*. However, this is not instantaneously but takes until the third exposure. In case of dithered observations, between dither points the detector is reset and goes into *resetting equilibrium* again. The result is that images 1, 2 and 3 of each dither point differ in image background, and the sky background must be determined separately for the three groups of images. Images after the third exposure share the same image background as the third image.

The bias and dark levels of LIRIS are unstable over time, as is the case for most near-IR detectors. Therefore directly before each exposure a bias image is taken and subtracted automatically from the actual exposure. The dark current of LIRIS is small and usually subtracted from the data in the sky subtraction.

2.1.2 Dither pattern/exposure time

Even at night the atmosphere radiates enough in infrared to saturate the detector in short timespan, the CCD saturates in around 40 seconds due to the sky background. Bright objects may saturate in a shorter period, which could be the case for stars from the 2MASS catalogue, necessary for photometry. In order to make deep observations many exposures are necessary. To be able to observe sources up to 21^{th} magnitude in infrared with LIRIS a total exposure time of roughly an hour is needed at good (0.7″) seeing. With an exposure time of 15 s for a single image this means at least a total of 240 images per source is needed, depending on seeing conditions. The exposure time is a compromise between exposure efficiency and accounting for the sky background. A shorter exposure time means that more images are needed, so overhead costs a lot more time. Longer exposures will cause saturation of reference stars that are necessary for photometry, and make a dither cycle too long with respect to the timescale of sky background variation.
Apart from many short exposures the images are also dithered. Dithering images means introducing small shifts in the pointing of the telescope after a set number of exposures. The main reason is to be able to construct a sky image, necessary for data-reduction, this will be treated in the next section. By dithering a given source is imaged onto different parts of the detector, while artifacts associated with the detector are not. Median combining dithered images then helps in artifact detection and compensation for flat-field effects. The exposures follow a dither pattern of 5 positions, where at each dither position 5 images are taken. The dither offsets have a step-size of 12″ so they largely overlap (see Fig. 2.1). The exposure time for an image is set at 15 s, in order to have a deep image without saturating the reference stars needed in the photometry later. So one cycle consists of 25 images and a total exposure time of 375 s. Usually 10 cycles are needed for a single source, or more in case of poor seeing.
Special care is taken in positioning the location of the ULX on the detector. The position of the ULX was chosen such that we maximize the number of 2MASS stars for astrometry and photometry and maximize the area free of background from the host galaxy. Then care was taken that the ULX was not positioned near the edge of the detector, otherwise some dither positions might not cover it, and bad pixels on the detector are mostly located near the edge. One also does not want the ULX to fall on the border between the quadrants, so the ideal position is in the center of a quadrant. What quadrant depends on the position of the ULX with respect to its host galaxy, since an uncrowded field makes data reduction more successful. The quadrants refer to the four read-out quadrants of the detector.

2.2 Data reduction

2.2.1 THELI package

Data obtained with LIRIS can be fully reduced with the data reduction package THELI [20]. THELI is suitable to reduce data from a large number of instruments. This software produces a calibrated stacked image based on a set of raw images. It also allows for splitting the data and treating groups of images separately, which is crucial due to the reset anomaly explained earlier. The sky background fluctuates significantly in infrared on a timescale of ∼10 minutes. To take that into account each cycle of 25 images is reduced separately. Each night just after sunset a large number (150-200) of sky-flats are taken, out of which

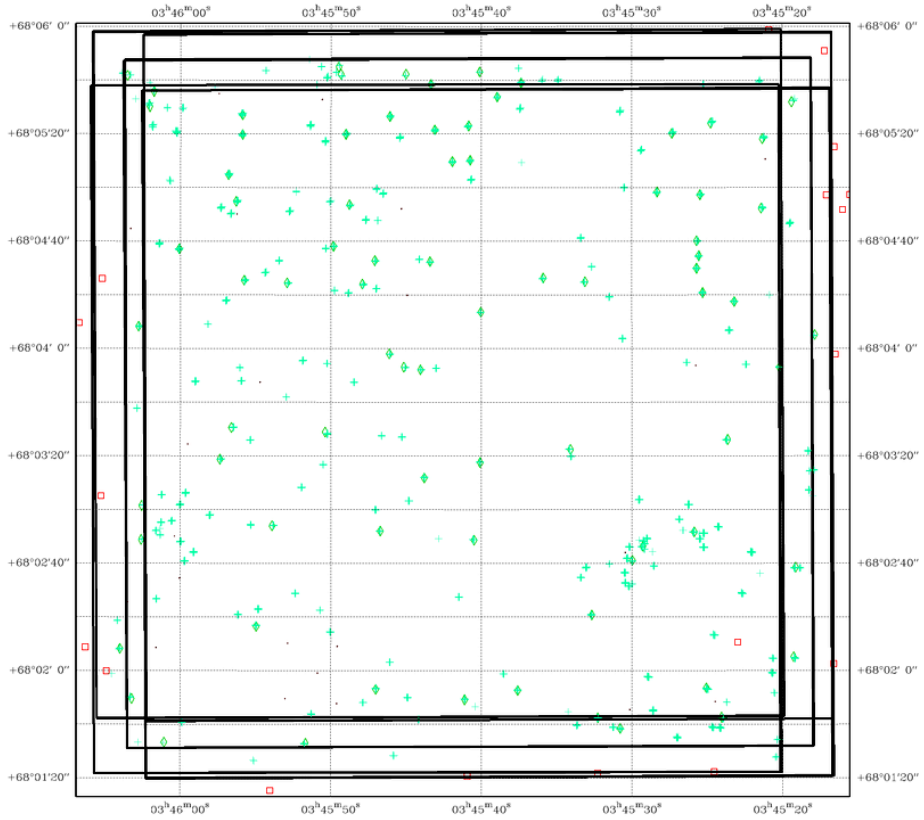

Figure 2.1: THELI check-plot shows the dither pattern for an IC-342 X-1 cycle. The boxes show the overlapping dither positions. The green dots display the matched reference sources and the red dots the unmatched. The coordinates of the field of view are as indicated.

∼30-50 non-saturated flats are selected as input for the flatting procedure. Most of the parameters in the software are automatically set to the correct value after selecting the proper instrument (LIRIS).

Flatfielding and superflatting in Theli

After selecting the proper instrument the sky-flat exposures are median combined into a masterflat. The images are then split into three groups to be reduced separately due to the reset anomaly. The masterflat is then applied on the data to remove artifacts that are caused by variations of pixel-to-pixel sensitivity of the detector and other distortions or cosmetic features. No bias is subtracted since that was already automatically done by the observing system software. A superflat, the sky background model in THELI, is created which is necessary since in the near-IR the sky changes constantly and results in large background variations. Since the sky varies on a timescale of ∼10 minutes and one cycle accounts for roughly six minutes of exposure time, a single (static) superflat can be based on all exposures of that cycle. To make a superflat first all objects are detected and masked by use of the SExtractor software [21], then the remaining images are rescaled and median combined. The superflat will subsequently be subtracted from the images. After this step the three groups of images are merged again to be treated the same in the final steps. Remaining reset anomaly residuals, that show as a background gradient with a discrete jump from the lower to the upper half of the image, are removed by collapse correction. Here an average column is calculated from all rows and the average profile is subtracted from each column. An example of a raw image and the image after data reduction is shown in Fig. 2.2 and 2.3.

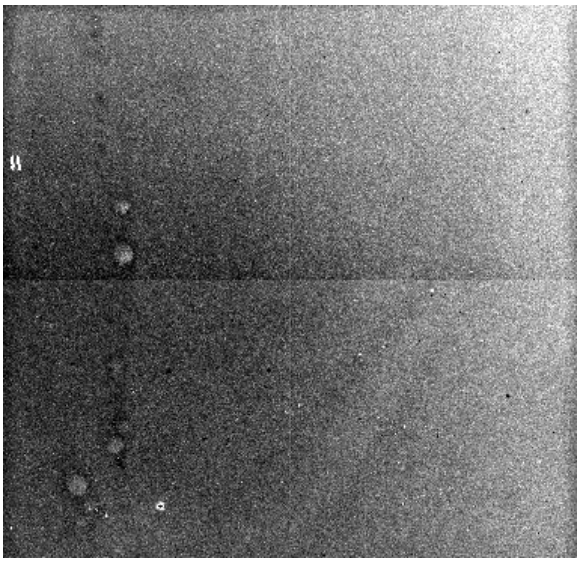

Figure 2.2: An inverted single raw image of NGC 925. Note the scratches on the far left, a bright spot surrounded by dark pixels in the lower left quadrant and the larger spots on the left side on the image.

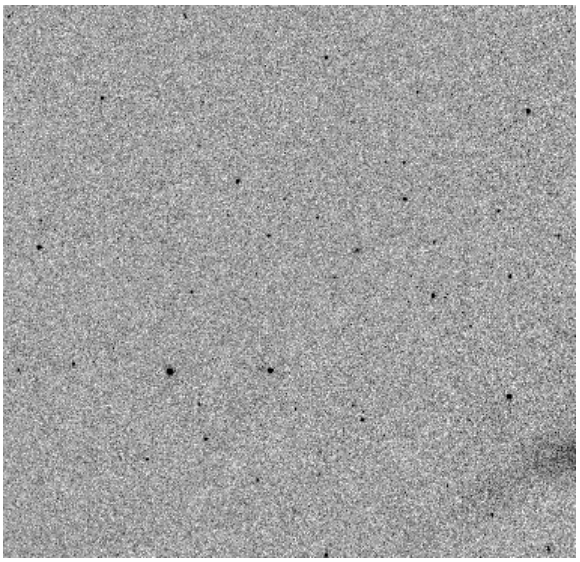

Figure 2.3: The fully reduced image of Fig. 2.2 on the left side. All detector flaws have been removed and sources are now visible. The dark region in the lower right is the host galaxy NGC 925.

Astrometry in THELI

The next step in THELI is the astrometry section. Here SExtractor is used for object detection and the program SCAMP to obtain a astrometric solution [22]. From the detected objects a source catalogue is created for every exposure. Based on this source catalogue SCAMP offers an astrometric solution including distortion correction. This solution is the result of a χ^2 minimization, with χ^2 the quadratic sum of differences in position between overlapping detections from two fields. One field is the catalogue created by SExtractor and the second a reference catalogue selected in the THELI software. Preferably the 2MASS-catalogue [23] is selected, but often not enough known 2MASS sources are located in the field of view of the images. In that case, either the SDSS-DR8 [24] or USNO-B1 catalogue [25] is used. If a solution is found, the astrometry from the reference catalogue is applied to the image. This is done for every image individually. To check if the solution is correct, several check-plots are available. The most important one shows the borders of all images with respect to each other, together with unmatched and matched detections. In case of a correct solution, the dither pattern should be discernible in this checkplot (see Fig. 2.1).
In case SCAMP fails to come up with a solution or the solution is incorrect, several parameters can be adjusted to solve the issue. The offset of the detection pointing can be deduced from the images by loading the reference catalogue in the image with DS9 [26], and comparing these by eye with the observed sources. Based on this the maximum uncertainty in the pointing can be limited. The object detection by SExtractor can be checked similarly, by loading the created source catalogue in the images. Tuning the object detection thresholds helps SCAMP to come up with a (better) solution.

Coaddition

In the final step the images are coadded. First remaining sky residuals are subtracted by running SExtractor to remove all objects from the image after which the result is smoothed and subtracted. Then the images are resampled to a common output grid taking into account the astrometric solution for every image calculated previously. Finally the resampled images are coadded using the program SWARP [27] and the final coadded image

is updated with the proper WCS coordinates and other parameters. Since the cycles are coadded individually and not a lot of variation is expected over the duration of a cycle, the average over all exposures is taken to create the final image of a cycle.

2.2.2 Exceptions

Not all observations were reduced and coadded successfully with THELI. This was mostly due to a lack of reference stars in the field of view in the available catalogues, so no astrometric solution could be found. Since the coaddition in THELI relies on the astrometry in the individual frames, coaddition was also not possible. In one case, for M74, this was solved by creating a reference image with known astrometry to replace a reference catalogue, but for the other cases another method for astrometry and coaddition was necessary. The data reduction process in THELI was successful for all observations, so the reduced images of the observations with no succesful coaddition were extracted from THELI for alternative astrometry.
First the images of the cycles, for which THELI could not find an astrometric solution, need to be aligned before they are coadded. The task *Xregister* in IRAF[1] computes the shift in x and y for a set of images in reference to one of the images. These translations are based on cross-correlation of shared features and the output is a shifted image for every input image. A region is specified which is used for computing the cross-correlation function shifts, that should include at least one shared well-defined object. The algorithms used to compute the cross-correlation function are either a discrete function, where a discrete convolution of the reference and input image is computed, or a Fourier function, where the convolution is based on Fourier techniques. The choice of algorithm depends on the set of input images. The shifted images are then median combined using the task *Imcombine* in IRAF. The same procedure is repeated for the combined images of each cycle of a source. So if an observation consists of 10 cycles of 25 images each (5 exposures at 5 dither points), first every cycle of 25 images is shifted and combined, and then the ten resulting images are combined the same way. Since THELI, when successful, produces a stacked image for each cycle, they too need to be combined following the same procedure of *Xregister* and *Imcombine*.
For one set of data, NGC 4618, neither method of coaddition described here proved successful. This was due to a lack of catalogue stars in the field of view and lack of a bright common source for the alignment.

2.2.3 Astrometry

The final images of THELI already have astrometry, since all the individual images are fitted to reference catalogues prior to coaddition. The coadded images that are the result of the second method do not have proper astrometry yet. This is done by use of the programs DS9 and STARLINK-program GAIA. Since the 2MASS catalogue did not have enough sources in the field of view in THELI, a different catalogue is needed to obtain the coordinates of enough sources to make a reliable fit. DS9 offers the SDSS-catalogue, which in all cases has enough reference stars in the field of view.[2] By loading the stacked image in DS9, and then loading the reference catalogue in the image, it is an easy matter to identify the catalogue counterparts to the sources visible in the image. In GAIA with the task *Pick object* these sources can be selected, and the coordinate information obtained in DS9 added for a number of stars, between 5-10. GAIA calculates a fit based on this input and the

[1] IRAF is distributed by the National Optical Astronomy Observatory, which is operated by the Association of Universities for Research in Astronomy (AURA) under cooperative agreement with the National Science Foundation.

[2] As stated earlier THELI also offers the SDSS-catalogue. In a lot of cases astrometry based on this catalogue in THELI was successful. But nothing is ever easy, and for a number of sources SCAMP could not find a proper astrometric solution, whereas doing this manually using DS9 provided a solution.

astrometry is saved if the root mean square (rms) of the fit is satisfactory ($\lesssim 0.25''$).
At this point the images for each source are successfully stacked and have astrometry. Now it is time to see if there are any detections in the K_s-band at the locations of the ULXs. The positions of the ULXs are provided in two recent publications based on observations with XMM-Newton [28] and Chandra [29]. The Chandra catalogue includes 107 ULXs with luminosities in excess of 10^{39} erg s^{-1} that are identified in a complete sample of 127 nearby galaxies. The XMM catalogue lists 470 ULX candidates located in 238 nearby galaxies, by cross-correlating the 2XMM Serendipitous Survey with the Third Reference Catalogue of Bright Galaxies. The error on the coordinates depend on the catalogue used, this will be treated in the section *Error analysis*. If there is a detection within the error circle we want to know what the apparent magnitude of this detection is. In case of a non-detection it is important to know to what magnitude a source would have been detected, to set a lower limit to the apparent magnitude of a potential detection. In order to calculate this we need to do photometry.

2.2.4 Photometry

To calculate the apparent magnitude of a detection, its instrumental magnitude in the image is compared to another source of known magnitude detected in the same image. If the instrumental magnitude of the detection and of a reference star in the image are known, as well as the known apparent magnitude of the reference star, the apparent magnitude of the detection can be easily calculated:

$$m_d = I_d + (m_{ref} - I_{ref}) \tag{2.1}$$

where I_d and I_{ref} are the instrumental magnitudes of the detection and the reference star, and m_d and m_{ref} the apparent magnitudes of the detection and the reference star. The reference stars are selected from the 2MASS catalogue. To obtain the instrumental magnitude of the detection and the reference star(s) in the image the IRAF package DAOPHOT is used [30]. With the task DAOEDIT it is possible to obtain essential parameters like the full width at half maximum (FWHM) and the coordinates of the sources of interest. With the same task it is also possible to get an indication of the variability of the sky, *sky sigma* in Table 2.1. These parameters are necessary input for the task DAOPHOT. The important parameters necessary for task DAOPHOT are listed in Table 2.1. In this table *nr. of images* refers to the number of images the stacked image is composed of and *read-noise*$_L$ and *gain*$_L$ are the readnoise and gain of LIRIS (3 e^- and 3.6 e^-/ADU respectively). The centering algorithm is set at *centroid*, here the object centers are determined by computing the intensity weighted means of the marginal profiles in x and y, within the region set by the *centering box*. Because the images are fully reduced the average sky value is set at 0 and the sky fitting algorithm at constant.
Running DAOPHOT gives the instrumental magnitudes of the sources whose coordinates are provided, which then can be used to calculate the apparent magnitude of the detection.
To make sure the 2MASS reference star, that is used to determine the magnitude of the detection, is reliable, two other 2MASS stars in the field of view are used as comparison stars. Their apparent magnitudes are calculated in the same way as the detection by use of equation 2.1 with I_{ref} and m_{ref} the instrumental and apparent magnitude of the reference star, and I_d the instrumental magnitude of the comparison star. The resulting apparent magnitude is compared to the catalogue value to check if there is not a large discrepancy. A significant difference between the calculated and catalogue value of the comparison star could mean that either the reference or comparison star does not meet the desired standards. Reference and comparison stars should be non-saturated (so that they are within $< 2\%$ linearity) and a safe distance from the border of the stacked image so that it is certain all dithered images contribute to the brightness of the star.

Parameter	Value	IRAF task
FWHM	-	DAOEDIT
Sky sigma	-	DAOEDIT
Read-noise	$\sqrt{\text{nr. of images}} \times \text{read-noise}_L$	DAOPHOT/DATAPARS
Gain	$\text{gain}_L \times$ nr. of images	DAOPHOT/DATAPARS
Exposure time	15 s	DAOPHOT/DATAPARS
Centering algorithm	Centroid	DAOPHOT/CENTERPARS
Centering box	2 × FWHM	DAOPHOT/CENTERPARS
Sky fitting algorithm	Constant	DAOPHOT/FITSKYPARS
Skyvalue	0	DAOPHOT/FITSKYPARS
Aperture	FWHM+1	DAOPHOT/PHOTPARS
Sigma threshold	4	DAOFIND/FINDPARS

Table 2.1: Input obtained by DAOEDIT or necessary for DAOPHOT and DAOFIND. *nr. of images* refers to the number of images the stacked image is composed of and *read-noise*$_L$ and *gain*$_L$ are the readnoise and gain of LIRIS.

Finally for the detected sources the absolute magnitudes can then be calculated by the standard formula:

$$M = m - 5((\log_{10} D) - 1) \tag{2.2}$$

with M the absolute magnitude, m the apparent magnitude and D the distance to the host galaxy in parsecs.

Upper limit of a non-detection

For a source with a non-detection it is important to know to what magnitude a source would have been detected. If a coadded image shows sources up to 20^{th} magnitude, it can be concluded in case of a non-detection that the apparent magnitude of the ULX in K_s is fainter than this magnitude. Since the next step in identifying counterparts would be to take a spectrum of a high enough resolution, which in infrared is currently possible up to roughly 20^{th} magnitude, it means that that particular ULX is not a priority for further investigation. If due to bad seeing during the observing night a stacked image only goes as deep as for instance 18^{th} magnitude, it is sensible to try the observation again, even in case of a non-detection.
For the upper limit we use the magnitude of a detection of an isolated single source with an uncertainty in magnitude of 0.3, which corresponds roughly to a 3σ-detection. To find the instrumental magnitudes of these sources the task DAOFIND is used to identify all objects in the field of view up to a given sigma threshold, which is set at 4, see Table 2.1. Running DAOPHOT, with as input the coordinates of all identified sources, gives the instrumental magnitudes plus the error in magnitude for all sources. The magnitudes of several sources with error $\sim$0.3, combined with known magnitudes of the reference stars, are then used to deduce the upper limit of the image, through use of equation 2.1.

2.3 Error analysis

The error in the absolute magnitude of a detected source depends on both the error in the apparent magnitude of the detection and the error in the distance modulus of the associated galaxy. The final error in the absolute magnitude is then obtained by calculating the square root of these quadratically added errors.
The error in the distance modulus is based on the standard deviation of the mean of the distance determinations as found in the NASA/IPAC Extragalactic Database (NED)[3]. The error in the apparent magnitude is based on the errors in the instrumental magnitudes of both the detection as well as the reference source, and the error in the apparent magnitude of the reference source (see equation 2.1). The instrumental magnitudes are obtained by IRAF task DAOPHOT, as explained earlier, which output includes an error in the magnitudes. The error in the apparent magnitude of the reference source is based on the error provided in the 2MASS catalogue.
There is also an uncertainty in the zero-point calibration in the determination of the apparent magnitudes. The reference star used to calculate the apparent magnitude of a detection is calibrated by use of two other stars in the same field. The difference in the instrumental magnitudes of the reference and comparison stars may differ slightly from the difference in apparent magnitudes of the related stars in the 2MASS catalogue. This difference could be due to the uncertainties in the 2MASS magnitudes, which are larger for fainter sources. The color dependent transformation between the LIRIS K_s-filter and the 2MASS K_s-filter, while small, could also contribute:

$$(K_s)_{2MASS} = K_{MKO} + (0.002 \pm 0.004) + (0.026 \pm 0.006)(J - K)_{MKO} \tag{2.3}$$

where *MKO* is short for Mauna Kea Observatory, the photometric system of LIRIS' filters. Finally the discrepancy could also be a result of intrinsic variability of the 2MASS stars. Many stars are variable to some extent, and that variability will not show up in the catalogue since it is based on short snapshots. This calibration uncertainty that arises from the difference between derived magnitudes and the catalogue magnitudes should be taken into account, when calculating the apparent magnitudes. In general the error arising from this magnitude discrepancy is much larger than the errors in the instrumental magnitudes (factor ~ 100).
The X-ray positions of the ULXs are from either the XMM-Newton catalogue or the Chandra catalogue. The error in the catalogue X-ray position and the error of the astrometry fitting are quadratically added to obtain the radius of the error circle of the X-ray position in the coadded image. The overall 90% uncertainty circle of a Chandra X-ray absolute position has a radius of $0.6''$ and for XMM varies between $2''$ and $5''$ and is in general the dominant contribution to the total error. In principle the uncertainty of the stellar positions in the catalogue that the images are fitted to should also be taken into account, but this error is negligible compared to the distance and fitting errors and does not contribute significantly to the total position error.

[3]The NASA/IPAC Extragalactic Database (NED) is operated by the Jet Propulsion Laboratory, California Institute of Technology, under contract with the National Aeronautics and Space Administration.

Chapter 3

Results

During 5 nights in January 2012 we observed a total of 23 ULXs in the K_s-band. For 6 of those a detection was found within the error circle of the X-ray position of the ULX. The remaining 17 coadded images showed no detection, see Table 3.1. Out of these non-detections for 5 sources some structure is visible, but not a clear isolated point source, indicated by *f.s.* (faint structure) in the table. The ULX in NGC 855 is located near the galaxy center which appears very bright in near-IR. A potential detection would not be discernible in the first place so this source was skipped in further photometry. The reference catalogues used for the astrometry are either 2MASS, USNO-B1 or SDSS DR-8. The coordinates in Table 3.1 are X-ray positions from the Chandra catalogue, with the exception of the X-ray position of X-2 in M74, which is from the XMM catalogue.

3.1 Image quality

The seeing conditions during the observing nights varied between 0.6″ and ∼4″. In case of bad seeing for most sources a new set of cycles was obtained in a night with better seeing. Almost all exposures were taken with the autoguider on, which prevents the exposures from shifting with respect to another during an observing run. In some cases reacquiring the guide star between dither points caused smearing of images, which was a problem for 1% of all images. Prior to coaddition these images were taken out, this is accounted for in the exposure times shown in Table 3.1. For each source a minimum of ten cycles was observed, which amounts to 3750 s exposure time. Some sources show a lower total exposure time. This is because not all cycles of these datasets were reduced and coadded successfully in the used software, for example due to clouds or astrometry errors.

Source	Detections	D (Mpc)	m_K		Seeing	T_{exp} (s)	Ref. catalogue	ULX X-ray position	
Detections								R.A.	Dec.
NGC 2500 X-2	Point source	10.1 ± 1.9	15.8 ± 0.1		0.7″	6750	USNO-B1	08:01:57.85	+50:43:39.50
NGC 925 X-1	Point source	8.6 ± 1.2	18.5 ± 0.1		0.6″	2715	2MASS	02:27:21.52	+33:35:00.70
NGC 1058	Point source	9.3 ± 3.9	19.2 ± 0.1		0.7″	5250	2MASS	02:43:23.27†	+37:20:42.11
Holmberg II X-1	Point source	3.3 ± 0.9	19.5 ± 0.1		0.9″	3750	USNO-B1	08:19:29.00	+70:42:19.30
NGC 925 X-2	Point source	8.6 ± 1.2	19.9 ± 0.1		0.6″	2715	2MASS	02:27:27.53	+33:34:43.00
M74 X-1	Point source	9.1 ± 1.1	20.0 ± 0.2		0.9″	6375	R-band image	01:36:51.08	+15:45:46.70
			Limit magnitude						
Non detections			m_K	M_K					
NGC 3239 X-1	No (f.s.)	8.1 ± 1.5	19.6	-9.9 ± 0.5	1.3″	2610	2MASS*	10:25:06.98	+17:09:47.20
NGC 3239 X-2	No	8.1 ± 1.5	19.6	-9.9 ± 0.5	1.3″	2610	2MASS*	10:25:08.20	+17:09:48.30
NGC 2403 X-1	No	3.6 ± 0.7	19.7	-8.1 ± 0.5	2.0″	5160	USNO-B1	07:36:25.53	+65:35:40.00
IC 342 X-2	No	3.6 ± 1.3	19.9	-7.7 ± 0.8	1.5″	3000	USNO-B1	03:46:15.64	+68:11:12.20
M81	No	3.7 ± 0.5	20.0	-7.8 ± 0.4	1.1″	3375	USNO-B1	09:55:32.97	+69:00:33.40
NGC 5474	No	6.5 ± 0.7	20.2	-8.8 ± 0.3	1.4″	3300	SDSS*	14:04:59.73	+53:38:09.10
NGC 2500 X-1	No	10.1 ± 1.9	20.5	-9.5 ± 0.5	1.4″	4875	USNO-B1	08:01:48.10	+50:43:54.60
IC 342 X-1	No (f.s.)	3.6 ± 1.3	20.5	-7.1 ± 0.8	0.6″	3750	2MASS	03:45:55.61	+68:04:55.30
NGC 4395	No (f.s.)	4.5 ± 1.1	20.8	-7.5 ± 0.6	1.1″	5625	SDSS	12:26:01.44	+33:31:31.10
NGC 3184	No	11.9 ± 2.7	21.0	-9.3 ± 0.5	1.0″	3240	USNO-B1	10:18:12.05	+41:24:20.70
NGC 5585	No	8.7 ± 1.1	21.0	-8.7 ± 0.4	1.3″	4650	USNO-B1	14:19:39.39	+56:41:37.80
NGC 3486	No (f.s.)	12.2 ± 3.5	21.1	-9.2 ± 0.8	1.1″	4515	SDSS*	11:00:21.76†	+28:58:18.04
NGC 2403 X-2	No	3.6 ± 0.7	21.1	-6.6 ± 0.5	0.9″	2625	SDSS	07:37:02.33	+65:39:34.96
NGC 4449	No (f.s.)	3.7 ± 0.6	21.3	-6.5 ± 0.5	1.0″	3375	SDSS*	12:28:17.83	+44:06:33.90
M74 X-2	No	9.1 ± 1.1	21.5	-8.3 ± 0.4	0.8″	8625	R-band image	01:36:36.40⋆	+15:50:36.00
NGC 855	No	9.7 ± 0.8	-	-	0.9″	4125	SDSS	02:14:04.08	+27:52:39.50
NGC 4618	-	7.3 ± 1.3							

Table 3.1: Results of data reduction and photometry of all observed ULX X-ray positions in the K_s-band. With D the distance to the host galaxy; m_K the magnitude in K_s of a detection or limit of a non-detection; M_K the absolute magnitude corresponding to the magnitude limit of a non-detection; T_{exp} the total exposure time; Reference catalogues as used in THELI for astrometry, where $*$ indicates a coaddition exception, see 2.2.2; ULX X-ray positions are generally from the Chandra catalogue, with ⋆=XMM position and †=updated Chandra position based on analysis by Peter Jonker, SRON. Errors in magnitude limits are ∼0.3 and the errors in the distances of the host galaxies are based on the standard deviation of the mean of the distance determinations as found in the NED.

Figure 3.1: The bright detection of 15^{th} magnitude at the position of ULX X-2 in NGC 2500. The host galaxy is partly visible in the upper right corner. On the right edge of the image a foreground star is visible which appears very bright in near-IR. The source is found in the SDSS catalogue with a magnitude in g of 19.2, which means the detection has a $V - K$ of 3.4, which fits well for a K-type star. The image is based on observations in the K_s-band with a total exposure time of 6750 s and seeing of 0.7″. Directions and scales are as indicated, size of blow-up box is 10″ by 10″. The error circle of 0.6″ represents the 90% confidence region of the ULX X-ray position. These scales and orientation apply to all figures.

3.2 Detections

Out of the 23 sources observed in 6 cases a detection was found within the error circle of the ULX X-ray position. The apparent and absolute magnitudes of these detections are shown in Table 3.2, as well as the distances to the (supposed) host galaxies. The distances to the galaxies are averages over the results of several studies as found in the NASA/IPAC Extragalactic Database (NED). The absolute magnitudes are calculated by use of equation 2.2.

As can be seen in Table 3.2 there is one detection significantly brighter than the other five. The detection at the coordinates of X-2 in NGC 2500 has a magnitude of 15.8 in the K_s-band and falls well within the X-ray coordinate error circle, as can be seen in Fig. 3.1. As in all the figures of detections the size of the enlarged blow-up is 10″ by 10″ and North is up and East to the left.

In NGC 925 two detections at two ULX X-ray positions are found in the same field of view, see Fig. 3.2. At X-ray position X-1 there is a bright detection of 18^{th} magnitude, which is located in a crowded field and slightly blended with a nearby object. At X-ray position X-2 the detection is much fainter at nearly 20^{th} magnitude and located at the edge of the error circle. The detections in NGC 1058 and Holmberg II are also of 19^{th} magnitude, but are much clearer single point sources well within the error circle, see Fig. 3.6 and Fig. 3.7. Finally the detection in M74 is very faint at 20^{th} magnitude and not a very clear point source, see Fig. 3.5.

Source	m_K	D (Mpc)	M_K	Ext. (pc)	Sep.	Chance Al.
NGC 2500 X-2	15.8	10.1 ± 1.9	-14.2 ± 0.3	36 (1.1)	0.7″	0.03%
NGC 925 X-1	18.5	8.6 ± 1.2	-11.1 ± 0.3	47 (2.0)	0.2″	0.48%
NGC 1058	19.2	9.3 ± 3.9	-10.6 ± 1.5	30 (1.0)	0.2″	0.42%
Holmberg II X-1	19.5	3.3 ± 0.9	-8.1 ± 0.7	19 (1.3)	0.1″	0.62%
NGC 925 X-2	19.9	8.6 ± 1.2	-9.7 ± 0.4	35 (1.5)	0.5″	2.53%
M74 X-1	20.0	9.1 ± 1.1	-9.7 ± 0.3	22 (0.6)	0.1″	6.34%

Table 3.2: Apparent and absolute magnitudes of the detected sources. With m_K the magnitude in K_s; D the distance to the host galaxy; M_K the absolute magnitude; Ext. the extension of the detection in parsec with in brackets the extension relative to an isolated point source in the same image; Sep. the separation between the detection and the ULX X-ray position in arcsecond. The errors in the absolute magnitudes are dominated by the error in the distances to the host galaxies, the reason why the errors on the apparent magnitudes are not given.

Figure 3.2: The detections at ULX X-ray positions X-1 (right) and X-2 (left) in NGC 925. The image is based on observations in the K_s-band with a total exposure time of 2715 s and seeing of 0.6″. The detection at X-ray position X-1 is of 18^{th} magnitude and slightly blended with a nearby source. At X-2 the detection is fainter, of nearly 20^{th} magnitude, and is located at the edge of the error circle. The host galaxy is visible in the lower right corner.

3.2.1 Extension and Separation

In Table 3.2 the extension of a detection is shown, which is orthogonal to the line of sight. This is based on the distance to the associated galaxy and the FWHM of the detection in arcsecond:

$$\text{Extension(pc)} = \text{FWHM}(″) * \text{D(pc)} * (\frac{1}{60 \times 60} \times \frac{\pi}{180}) \tag{3.1}$$

In brackets the extension relative to a single point source in the same image is given. The column *Sep.* of Table 3.2 shows the separation in arcseconds between the X-ray Chandra position associated with the ULX and the center of the detection.

3.2.2 Chance Alignment

Table 3.2 also gives the chance alignment of the detection in the last column. There is a possibility that a source falls within the error circle of the ULX X-ray position as a result of random distribution, a chance alignment. This source would then be considered a detection, while it might not be associated with the object that one is looking for. This is more likely to happen in a crowded field, where the stellar density, the number of sources per arcsecond squared, is higher. A chance alignment is expressed as a percentage and is calculated as the stellar density of sources of the magnitude of the detection or brighter times the surface of the error circle in which a source would be considered a detection. So a chance alignment of one percent means that out of hundred detections one happens to be in the error circle by chance.
The radius of the error circle is for all detections dominated by the error in the X-ray

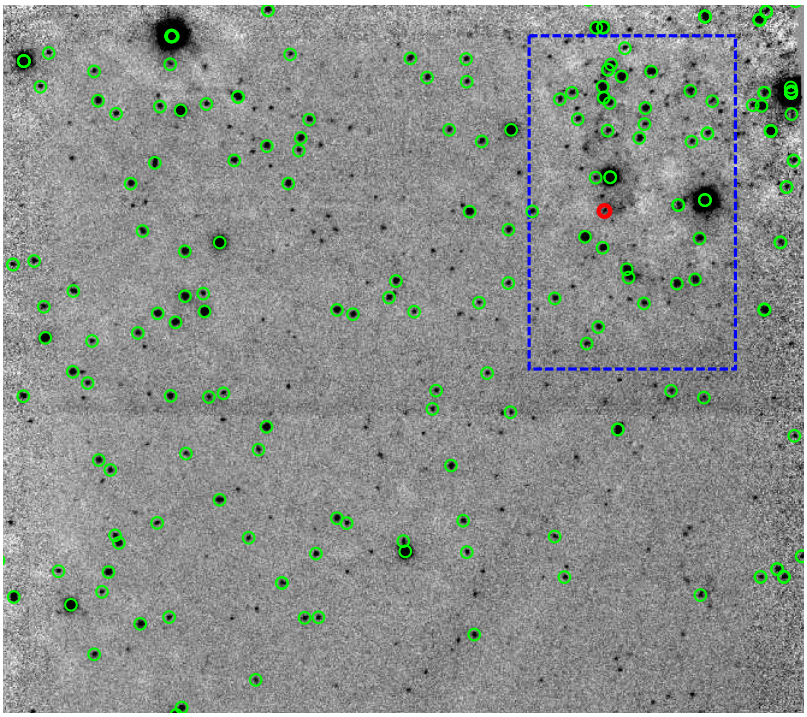

Figure 3.3: An example of a field used to obtain the stellar density necessary for chance alignment, in this case for the detection at X-ray position X-1 in Holmberg II. The field borders are indicated by the blue dashed box. The green circles represent sources at least as bright as the detection at X-ray position X-1, indicated by the red circle. Note the lower stellar density in the image in the regions further away from the host galaxy, which is situated in the direction of the upper right corner.

position of the ULX from the Chandra catalogue and is 0.6″-0.7″. To obtain the stellar density a field in the image is chosen around the detection that is homogeneous and typical to the immediate surroundings of the detection. Stellar density is variable and is highly dependent on the location with respect to the host galaxy. In the galaxy center it will be much higher than in an empty field far from the galaxy. When a field is established IRAF task DAOFIND is used to identify sources and DAOPHOT to calculate their magnitudes. To obtain the stellar density of this field only sources with a magnitude of the detection or brighter are used. Fig. 3.3 of Holmberg II shows an example of a homogeneous field used to calculate the stellar density. The blue dashed box shows the borders of this field. The green circles indicate the positions of sources at least as bright as the detections magnitude that also satisfy the DAOFIND parameter *Sigma threshold*, see Table 2.1. To make sure DAOFIND picks up the detection in this case this is set at either 2 or 3, depending on the faintness

of the detection. The red circle indicates the position of the detection. The selected field around the detections in NGC 1058 is similar to the one in Fig. 3.3 of Holmberg II. In case of NGC 2500 the detection at X-ray position X-2 is so bright that it is unlikely to be associated with the host galaxy, this will be treated in the next chapter. Therefore the field chosen can safely include most of the image to pick up the few stars with a brightness as high as the detection. In case of the detections at the X-ray positions X-1 and X-2 in NGC 925, they are located in one of the star-dense spiral arms of the galaxy. The field is chosen to cover this spiral arm, see Fig. 3.4. This of course results in a relatively high chance alignment, since the field is restricted to a star-dense region. Taking into account that the position of these detections mean that they are more likely to be spatially related to the spiral arm than to be a foreground or background source, the chance alignment should be taken as a conservative percentage. The same reasoning applies to the detection at X-1 in M74, which is located amidst several OB-associations [31]. The field chosen in this image covers only this star-dense region. In Table A.1 in Appendix A for every detection the location and dimension of the chosen field is given.

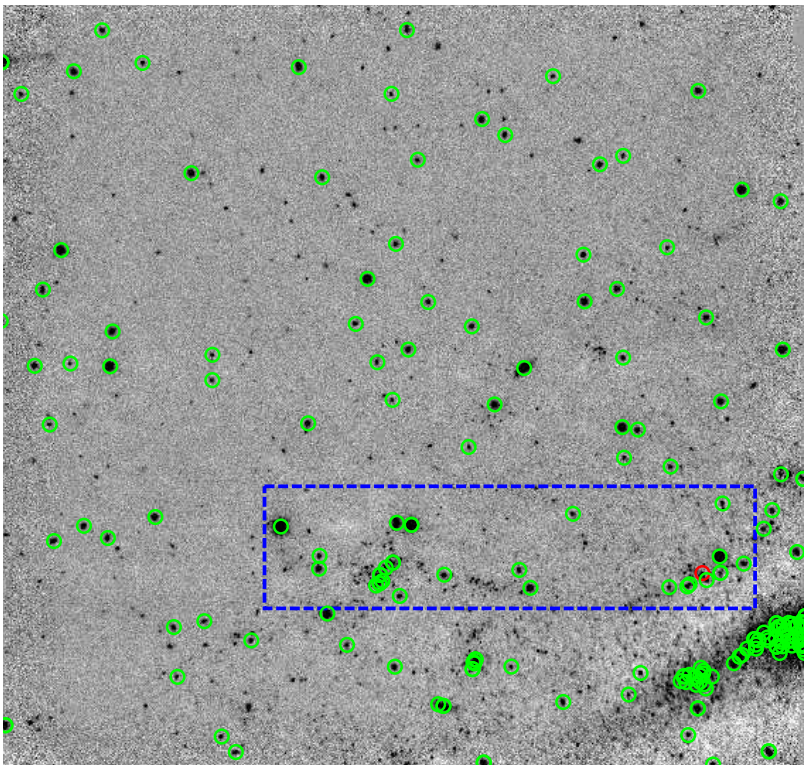

Figure 3.4: The field of stars used for chance alignment for the detection at X-ray position X-1 in NGC 925. The field borders are indicated by the blue dashed box. The green circles represent sources at least as bright as the detection at X-ray position X-1, indicated by the red circle. The field is chosen to include the spiral arm where the detection is located, but exclude the galactic center and the the unresolved region around it in the lower left corner. The detection at X-ray position X-2 is not indicated in this image. Since this detection is much fainter than the detection at X-1, the number of stars at least as bright is much higher, but it follows the same galactic structure as seen here.

Figure 3.5: The faint detection at the ULX X-ray position X-1 in M74, of 20^{th} magnitude well within the error circle. A part of the host galaxy is visible on the upper right corner of the image. The image is based on observations in the K_s-band with a total exposure time of 6375 s and seeing of $0.9''$.

Figure 3.6: The detection at the ULX X-ray position in NGC 1058, a clear isolated single source of 19^{th} magnitude well within the error circle. The host galaxy is visible on the left edge of the image. The image is based on observations in the K_s-band with a total exposure time of 5250 s and seeing of $0.7''$.

Figure 3.7: The clear isolated single detection at ULX X-ray position X-1 in Holmberg II, of 19^{th} magnitude. The host galaxy is visible at the upper right corner. The image is based on observations in the K_s-band with a total exposure time of 3750 s and seeing of $0.9''$.

3.2.3 Limiting magnitude

The other 17 observed sources did not show a clear isolated point source, but 5 images did show some faint structure around the ULX X-ray position. An example of a faint structure is shown in Figure 3.8 at X-ray position X-2 in IC 342, where there is some structure visible around the edge of the error circle of the X-ray position. There is also some structure visible near the center, but this was too faint to calculate a magnitude. Figure 3.9 of NGC 2403 is an example of a clear non-detection with no structure visible at all in the K_s-band near ULX X-ray position X-2. For all sources with non-detections it is important to know to what magnitude a counterpart candidate would have been detected. As described earlier the limiting magnitude is set at the magnitude where a detection has a magnitude error of $\sim$0.3. In Table 3.1 the limiting magnitudes are shown. The limit magnitude is the highest for M74 X-2, which you would expect based on the largest exposure time and good seeing conditions. Also unsurprisingly is the low limit magnitude for NGC 3239, since this data set is obtained during one of the worst seeing conditions and also has the lowest exposure time. In the next column the absolute magnitudes that correspond to a detection at the limit magnitude are shown.

Figure 3.8: An example of a faint structure on the edge of the error circle around ULX X-ray position X-1 in IC 342. There is some structure visible within the error circle, but this was too faint to calculate its magnitude with IRAF task DAOPHOT. The host galaxy is in the direction of the upper left corner of the image. The image is based on observations in the K_s-band with a total exposure time of 3750 s and seeing of 0.6″.

Figure 3.9: An example of a clear non-detection at ULX X-ray position X-2 in NGC 2403, where the host galaxy in direction of the the lower right corner. The image is based on observations in the K_s-band with a total exposure time of 2625 s and seeing of 0.9″.

Chapter 4

Discussion

4.1 Candidate counterparts

The overall goal of this research is to determine the mass of the black hole of a ULX by use of spectra of potential red supergiant donor stars. This thesis focuses on the first step towards this goal which is to identify viable infrared counterparts. A total of 23 ULXs were observed in the K_s-band during 5 nights between January 1st and January 8th, 2012, with LIRIS at the WHT. All observed ULXs are associated with galaxies at a distance $\lesssim$10 Mpc, to make sure that a possible detection of a counterpart would be bright enough for future spectroscopy. A detection was found at a total of 6 ULX X-ray positions, for which we determined the apparent and absolute magnitudes in the K_s-band, see Table 3.2. The remaining observed X-ray positions did not show a detection or only some vague structure and not a clear single point source, see Table 3.1. Out of the 6 detections 4 are clear point sources well within the error circle for the position, specifically at X-ray position X-1 in NGC 925, at X-1 in M74, at the X-ray position in NGC 1058 and at X-1 in Holmberg II, see respectively Fig. 3.2, 3.5, 3.6, and 3.7. The detection at X-ray position X-2 in NGC 925 is on the edge of the error circle, while the detection at X-ray position X-2 in NGC 2500 is a very bright extended source, see respectively Fig. 3.2 and 3.1.

4.1.1 Chance alignment and extension

It is possible that a source falls within the error circle of the ULX X-ray position as a result of chance alignment. In that case the detection is not associated with the X-ray source at that position and not a counterpart. For all the aforementioned detections we calculated the chance alignment, see Table 3.1. It is clear from the table that chance alignment percentages are somewhat correlated with the apparent magnitudes of the detections. This is not surprising since less stars are expected at brighter magnitudes. This is why the detection in NGC 2500 has such a low chance alignment, while the rest share similar values. As a result of the faintness of the detection and the location in a crowded region, the detections at X-2 in NGC 925 and at X-1 in M74 have a relatively high chance alignment, of a few percent. Still, this means in case of M74 X-1 that out of $\sim$15 similar detections, 1 happens to be there by chance. For the detections with a chance alignment of $\sim$0.5% this quickly runs up to 1 out of 200. Note that, as explained in section 3.2.2, the chance alignment of the detections in NGC 925 and M74 should be treated as a conservative value, since it is calculated based on the local star-dense region where the detections are located. This makes it likely that the source is associated with this region. In case of ULX X-ray position X-1 in M74 this conclusion is further strengthened by research by Krauss et al, who concludes, based on observations in optical, that it is unlikely to be a fore- or background source [31]. This makes the chance alignment of $\sim$6% of the M74 X-1 detection too

Spectral type	M_V	V-K	M_K
M0III	-0.4	3.85	-4.25
M7III	-0.3	7.7	-8.0
K0I	-6.0	2.15	-8.15
K5I	-5.8	3.5	-9.3
M0I	-5.6	3.8	-9.4
M5I	-5.6	5.2	-10.8

Table 4.1: Magnitudes and colors of K- or M-type giants and supergiants, as found in Allen's astrophysical quantities [33].

conservative.
The seeing for the images where the detections were found is in general in the order of $\sim 0.8''$, see Table 3.1. For ground-based observations in near-IR this is considered reasonably good seeing, but it puts restrictions on identifying the detections as single sources. Table 3.2 shows the extension of the detections in parsec and in brackets the relative extension compared to an isolated point source in the image. The more extended detections at the X-ray positions X-1 and X-2 in NGC 925 and at X-2 in NGC 2500 have diameters of around 35 pc, which would be considered small for an OB association but not impossible. In general OB associations have typical diameters of $\sim$80 pc. In NGC 925 the typical diameter is $\sim$90 pc, with a tail that extends to $\sim$30 pc [32]. The detections in NGC 925 also have an extension that is large relative to the seeing in the image, a factor of 1.5-2, which one would expect from a star cluster. Finally the bright absolute magnitude of -11.1 of the detection at X-1 in NGC 925 is consistent with the scenario that it is a star cluster, since it is very bright for a single source. The detections with smaller diameters of around 20 pc are much harder to explain by use of a star cluster and are likely to be single point sources, especially considering their relative extension of $\sim$1, as shown in Table 3.2.

4.1.2 Absolute magnitudes

In order to determine whether the magnitudes of these detections fit the properties of red supergiants we need to compare them to absolute magnitudes in the literature, see Table 4.1 (from Allen's astrophysical quantities [33]). As can be seen from Table 3.2 most detections have an absolute magnitude that falls well within the range of either a K- or an M-type supergiant. There are some exceptions. The absolute magnitude M_{K_s} of -8.1 of the detection at X-1 in Holmberg II could be explained as a $M7$-type giant or a K-type supergiant. On the other end the detection at X-ray position X-2 in NGC 2500 is so bright in K_s, with an absolute magnitude M_{K_s} of -14.2, that it is difficult to explain by use of any type of star. Interestingly this detection shows up in optical catalogues, with an apparent magnitude of 19.2 in g in SDSS [24]. Since it has an apparent magnitude of 15.8 in K_s, it has a $V-K$ of 3.4, which fits well for a K-type star. X-2 in NGC 2500 is likely a foreground X-ray source. Assuming the observed magnitude is due to a $K5$-type main sequence star, it would be located at a distance of $\sim$2 Kpc. Due to the extension of the source it could also be a star cluster related to NGC 2500 in which several giants contribute to the observed magnitude. Spectrometry is needed to verify the nature of this source.

4.2 ULX counterparts found so far

In total 3 detected sources, at X-1 in Holmberg II, at X-1 M74 and in NGC 1058 can be assumed to be new isolated single infrared ULX counterparts. The detections found

ULX X-ray source	m_V	Reference
Holmberg II X-1	21.6	Kaaret et al. 2004 [34]
Holmberg IX X-1	21.9	Grisé et al. 2011 [35]
IC 342 X-1	21.6	Feng & Kaaret 2008 [36]
M81 ULS1	21.7	Liu et al. 2008 [37]
M81 X-6	23.8	Liu et al. 2002 [38]
M101 ULX-1	23.2	Kuntz et al. 2005 [39]
NGC 1313 X-2	23.2	Ramsey et al. 2006 [40]
NGC 5204 X-1	22.5	Liu et al. 2004 [41]
NGC 5408 X-1†	22.1	Lang et al. 2007 [42]
NGC 6946 ULX-1*	21.3	Kaaret et al. 2010 [43]
M83 IXO 82	25.3	Tao et al. 2011 [44]
NGC 2403 X-1	24.6	Tao et al. 2011 [44]
NGC 4559 X-7	23.0	Tao et al. 2011 [44]
NGC 7793 P13	20.5	Motch et al. 2011 [45]

Table 4.2: Optical counterparts to ULXs found in literature. Values of m_V based on Tao et al. 2011 [44]. * indicates a UV counterpart, † a radio counterpart.

at ULX X-ray positions X-1 and X-2 in NGC 925 and at X-2 in NGC 2500 are possibly clusters, where observations with better angular resolution are needed to positively identify the ULX counterpart. The detection at X-2 in NGC 2500 could also be a foreground star. So far there are around 14 ULX counterparts identified in the literature, mainly in optical, and none in near-IR, see Table 4.2. So 3 new near-IR counterparts and 3 strong candidates means a significant increase in total known ULX counterparts, and a unique addition in near-IR. It should be mentioned that out of these 6 sources for 1 a counterpart already has been identified in optical, specifically Holmberg II X-1 [34].
This optical detection, on the same position of our near-IR detection, has a V magnitude of 21.64 ± 0.11, a colour $(B-V)_0 = -0.25 \pm 0.16$ and an absolute magnitude M_V between -5.5 and -5.9, depending on reddening within Holmberg II. This is consistent with a range of spectral types from O4V to B3Ib. However, the magnitude in K_s is 19.5 which means $V - K = 2.1$. Extinction in K is a fraction of V, so even with an uncertainty of 0.4 due to reddening in V within the galaxy, this is not consistent with these spectral types. These inconsistencies are likely due to the contributions of the disk in V, which was assumed to be not significant in the previously mentioned spectral classification. If the optical emission originates from the X-ray illuminated accretion disc, the magnitude in K_s can be an indication of a red donor-star.
According to research by Langer et al [46] the number ratio of blue-to-red supergiants appears to be an increasing function of metallicity. Assuming a supergiant is needed to fuel a ULX the number of observed counterparts in the K_s-band can give some insight in the relative ratio of red supergiants as donor stars in ULXs, and of the metallicity of the ULXs and their environment. In this case 23 ULXs were observed, with 6 detections of candidate counterparts. But a number of the observations that showed non-detections was inconclusive. So before something can be said about the relative supergiant ratio based on this sample, verification of these non-detections is needed. Even then the sample size is small, but combined with the aforementioned optical detections, it can provide valuable information on the matter of the blue-to-red supergiant ratio.

4.3 Non-detections

While a detection is of course the most interesting result in an image, a non-detection also provides valuable information. For a non-detection the limiting magnitude of the image is of most interest. The detection-limit of an image in case of no detection gives the lower limit of a potential detection in the K_s-band at the ULX X-ray position. Based on this information it could be decided to observe the source again in better conditions. Table 3.1 shows the limiting magnitudes of the images with the non-detections and the absolute magnitudes that are associated with these limit magnitudes. Since the goal of this research is to find possible red supergiants, we are interested in sources with an absolute magnitude of -8.1 to -10.8 in the K_s-band, see Table 4.1. So an absolute magnitude limit of -6.6 in K_s, in case of X-2 in NGC 2403, means that a counterpart would have been detected if the ULX contained a red supergiant. This is not the case and means that this source is of no further interest to this research. However, these absolute magnitude limits should be treated with care, since they are based on faint sources spread around the image. If the ULX X-ray position is located in a local crowded field, the absolute magnitude limit could be too optimistic for that region because of the higher local background. The X-ray positions X-1 and X-2 in NGC 3239 are for example located in an unresolved region of the image that is bright compared to the overall background of the image, which means that the calculated limit of -9.9 for this image is a conservative value for the region where the ULXs are located. The limit is for this region likely even fainter. This means that the obtained image is inconclusive and only a new observation can verify whether counterparts to these ULXs can be found in near-IR. To less extent the same reasoning applies to a number of other sources. They share a faint absolute magnitude limit and a ULX X-ray position in an unresolved region with a unreliable background. This is the case for NGC 3486, NGC 3184 and X-1 in NGC 2500.
The detections found in this study are in general found in images that are composed of exposures with good seeing conditions and long exposure times. Image quality increases with a smaller value of seeing and the depth of an image improves with longer exposure times. When sorting all observed sources by a value that takes into account both these properties, by dividing total exposure time by the FWHM of the stars in the image, it turns out the images that contain the 6 detections are all found in first 8 images. That the detections are found in deep good quality images is of course not surprising, but it also shows the necessity to review sources with shallow poor quality images.
Finally the ULX X-ray position X-2 in M74 is based on the XMM-catalogue, which can have an error in the position as large as 5″. There are two detections visible within 3.5″ of the X-ray position and more accurate observation in X-ray is needed to verify the position of the ULX in greater detail.

4.4 Future work

The 3 detections that have a large enough extension that they are possibly star clusters, first need to be observed with better angular resolution to positively identify the ULX counterpart. This can for example be done with a space-based telescope like the HST or a ground-based telescope that incorporates adaptive optics. The Gemini Near Infrared Imager (NIRI) can produce K-band images with a spatial resolution better than 0.2″. The non-detections that are inconclusive as a result of poor seeing conditions need to be observed again in the near-IR. Priority have the sources that are specified in section 4.3.
The next step after the successful identification of infrared counterparts to 6 ULXs is to obtain spectra to be able to identify unambiguously the donor star in the counterparts. This

will be followed by obtaining time-resolved photometric and spectroscopic observations in the infrared in order to deduce the masses of the black holes of the ULXs. This is not trivial, since the detections have magnitudes between 19.2 and 20 in the K_s-band, which is for ground-based telescopes around the limit of what is achievable nowadays. Given good conditions and a total integration time of 5 hours it is possible to obtain a K-band spectrum with a signal-to-noise of 10 of a source with an apparent magnitude of 19.5 using the Gemini NIRI spectrograph[1]. Several observations are needed during one period of a binary system to obtain the necessary orbital parameters in order to calculate a mass limit of the black hole. Because of the faint apparent magnitudes of the detections, total exposure times in the order of hours to days are necessary. The period of a ULX will most likely be long enough, due to the large masses of the black hole and donor star, that such long integration times will still produce detectable spectral line shifts.
Also new imaging observations in K_s of the found counterparts can shed light on the variability of the sources. This variability can be caused by ellipsoidal modulation, assuming the donor star fills its Roche lobe. However the amplitude of this effect might be too minor to observe, because the separation of the objects of a system with a long period will be large and the deformation of the donor star therefore small. Another cause of variability could be a change in accretion by the disk, which would give information about the nature of the ULX. Finally observations of a counterpart in other wavelengths might prove useful in the determining the nature of the ULX, as in the case of Holmberg II X-1, see section 4.2.

[1]For the integration time calculator (ITC) see http://www.gemini.edu/sciops/instruments/niri/itc-sensitivity-and-overheads

Appendices

Appendix A

Chance alignment details

Source	Chance Al.	Coordinates field center	Fieldsize (x)	Fieldsize (y)
NGC 2500 X-2	0.03%	08:02:03.48 +50:41:58.10	240″	225″
NGC 925 X-1	0.48%	02:27:26.79 +33:35:09.78	168″	42″
NGC 1058	0.42%	02:43:21.95 +37:20:29.97	87″	124″
Holmberg II X-1	0.62%	08:19:27.08 +70:42:22.28	70″	113″
NGC 925 X-2	2.53%	02:27:26.79 +33:35:09.78	168″	42″
M74 X-1	6.34%	01:36:51.31 +15:45:48.91	45″	39″

Table A.1: Chance alignment for each detection, with the center, width and length of the field.

Acknowledgments

We thank Mischa Schirmer for his very useful help with the data reduction software THELI. EK thanks Marianne Heida for her work during the observations on La Palma and for useful discussions.

Bibliography

[1] J. Frank, A. King, and D.J. Raine. *Accretion Power in Astrophysics*. Cambridge University Press, 2002.

[2] E. Körding, H. Falcke, and S. Markoff. Population X: Are the super-Eddington X-ray sources beamed jets in microblazars or intermediate mass black holes? *Astronomy and Astrophysics*, 382:L13–L16, January 2002.

[3] M. A. Abramowicz, B. Czerny, J. P. Lasota, and E. Szuszkiewicz. Slim accretion disks. *Astrophysical Journal*, 332:646–658, September 1988.

[4] S. Mineshige and K. Ohsuga. Supercritical accretion and ULXs - what can we achieve? *Astronomische Nachrichten*, 332:402, May 2011.

[5] M. C. Begelman. Super-Eddington Fluxes from Thin Accretion Disks? *Astrophysical Journal, Letters*, 568:L97–L100, April 2002.

[6] K. Belczynski, T. Bulik, C. L. Fryer, A. Ruiter, F. Valsecchi, J. S. Vink, and J. R. Hurley. On the Maximum Mass of Stellar Black Holes. *Astrophysical Journal*, 714:1217–1226, May 2010.

[7] J. A. Orosz, J. E. McClintock, R. Narayan, C. D. Bailyn, J. D. Hartman, L. Macri, J. Liu, W. Pietsch, R. A. Remillard, A. Shporer, and T. Mazeh. A 15.65-solar-mass black hole in an eclipsing binary in the nearby spiral galaxy M 33. *Nature*, 449:872–875, October 2007.

[8] P. Madau and M. J. Rees. Massive Black Holes as Population III Remnants. *Astrophysical Journal, Letters*, 551:L27–L30, April 2001.

[9] H. Feng and R. Soria. Ultraluminous X-ray sources in the Chandra and XMM-Newton era. *New Astronomy Reviews*, 55:166–183, November 2011.

[10] R. A. Remillard and J. E. McClintock. X-Ray Properties of Black-Hole Binaries. *Annual Review of Astronomy and Astrophysics*, 44:49–92, September 2006.

[11] N. I. Shakura and R. A. Sunyaev. Black holes in binary systems. Observational appearance. *Astronomy and Astrophysics*, 24:337–355, 1973.

[12] H. Feng and P. Kaaret. Identification of the X-ray Thermal Dominant State in an Ultraluminous X-ray Source in M82. *Astrophysical Journal, Letters*, 712:L169–L173, April 2010.

[13] T. Okajima, K. Ebisawa, and T. Kawaguchi. A Stellar-Mass Black Hole in the Ultraluminous X-Ray Source M82 X-1? *Astrophysical Journal, Letters*, 652:L105–L108, December 2006.

[14] P. Casella, G. Ponti, A. Patruno, T. Belloni, G. Miniutti, and L. Zampieri. Weighing the black holes in ultraluminous X-ray sources through timing. *Monthly Notices of the RAS*, 387:1707–1711, July 2008.

[15] J. Greiner, J. G. Cuby, and M. J. McCaughrean. An unusually massive stellar black hole in the Galaxy. *Nature*, 414:522–525, November 2001.

[16] M. W. Pakull, F. Grisé, and C. Motch. Ultraluminous X-ray Sources: Bubbles and Optical Counterparts. In E. J. A. Meurs and G. Fabbiano, editors, *Populations of High Energy Sources in Galaxies*, volume 230 of *IAU Symposium*, pages 293–297, 2006.

[17] J. Liu, J. Orosz, and J. N. Bregman. Dynamical Mass Constraints on the Ultraluminous X-Ray Source NGC 1313 X-2. *Astrophysical Journal*, 745:89, January 2012.

[18] T. P. Roberts, J. C. Gladstone, A. D. Goulding, A. M. Swinbank, M. J. Ward, M. R. Goad, and A. J. Levan. (No) dynamical constraints on the mass of the black hole in two ULXs. *Astronomische Nachrichten*, 332:398, May 2011.

[19] C. Copperwheat, M. Cropper, R. Soria, and K. Wu. Optical and infrared signatures of ultra-luminous X-ray sources. *Monthly Notices of the RAS*, 362:79–88, September 2005.

[20] T. Erben, M. Schirmer, J. P. Dietrich, O. Cordes, L. Haberzettl, M. Hetterscheidt, H. Hildebrandt, O. Schmithuesen, P. Schneider, P. Simon, E. Deul, R. N. Hook, N. Kaiser, M. Radovich, C. Benoist, M. Nonino, L. F. Olsen, I. Prandoni, R. Wichmann, S. Zaggia, D. Bomans, R. J. Dettmar, and J. M. Miralles. GaBoDS: The Garching-Bonn Deep Survey. IV. Methods for the image reduction of multi-chip cameras demonstrated on data from the ESO Wide-Field Imager. *Astronomische Nachrichten*, 326:432–464, July 2005.

[21] E. Bertin and S. Arnouts. SExtractor: Software for source extraction. *Astronomy and Astrophysics Supplement*, 117:393–404, June 1996.

[22] E. Bertin. Automatic Astrometric and Photometric Calibration with SCAMP. In C. Gabriel, C. Arviset, D. Ponz, and S. Enrique, editors, *Astronomical Data Analysis Software and Systems XV*, volume 351 of *Astronomical Society of the Pacific Conference Series*, page 112, July 2006.

[23] M. F. Skrutskie, R. M. Cutri, R. Stiening, M. D. Weinberg, S. Schneider, J. M. Carpenter, C. Beichman, R. Capps, T. Chester, J. Elias, J. Huchra, J. Liebert, C. Lonsdale, D. G. Monet, S. Price, P. Seitzer, T. Jarrett, J. D. Kirkpatrick, J. E. Gizis, E. Howard, T. Evans, J. Fowler, L. Fullmer, R. Hurt, R. Light, E. L. Kopan, K. A. Marsh, H. L. McCallon, R. Tam, S. Van Dyk, and S. Wheelock. The Two Micron All Sky Survey (2MASS). *The Astronomical Journal*, 131:1163–1183, February 2006.

[24] H. et al. Aihara. The Eighth Data Release of the Sloan Digital Sky Survey: First Data from SDSS-III. *The Astrophysical Journal Supplement*, 193:29, April 2011.

[25] D. G. Monet, S. E. Levine, B. Canzian, H. D. Ables, A. R. Bird, C. C. Dahn, H. H. Guetter, H. C. Harris, A. A. Henden, S. K. Leggett, H. F. Levison, C. B. Luginbuhl, J. Martini, A. K. B. Monet, J. A. Munn, J. R. Pier, A. R. Rhodes, B. Riepe, S. Sell, R. C. Stone, F. J. Vrba, R. L. Walker, G. Westerhout, R. J. Brucato, I. N. Reid, W. Schoening, M. Hartley, M. A. Read, and S. B. Tritton. The USNO-B Catalog. *The Astronomical Journal*, 125:984–993, February 2003.

[26] W. A. Joye and E. Mandel. New Features of SAOImage DS9. In H. E. Payne, R. I. Jedrzejewski, and R. N. Hook, editors, *Astronomical Data Analysis Software and Systems XII*, volume 295 of *Astronomical Society of the Pacific Conference Series*, page 489, 2003.

[27] E. Bertin. SWarp: Resampling and Co-adding FITS Images Together. *Astrophysics Source Code Library*, page 10068, October 2010.

[28] D. J. Walton, T. P. Roberts, S. Mateos, and V. Heard. 2XMM ultraluminous X-ray source candidates in nearby galaxies. *Monthly Notices of the RAS*, 416:1844–1861, September 2011.

[29] D. A. Swartz, R. Soria, A. F. Tennant, and M. Yukita. A Complete Sample of Ultraluminous X-ray Source Host Galaxies. *Astrophysical Journal*, 741:49, November 2011.

[30] P. B. Stetson. DAOPHOT - A computer program for crowded-field stellar photometry. *Astronomical Society of the Pacific, Publications*, 99:191–222, March 1987.

[31] M. I. Krauss, R. E. Kilgard, M. R. Garcia, T. P. Roberts, and A. H. Prestwich. M74 X-1 (CXOU J013651.1+154547): An Extremely Variable Ultraluminous X-Ray Source. *Astrophysical Journal*, 630:228–237, September 2005.

[32] F. Bresolin, R. C. Kennicutt, Jr., L. Ferrarese, B. K. Gibson, J. A. Graham, L. M. Macri, R. L. Phelps, D. M. Rawson, S. Sakai, N. A. Silbermann, P. B. Stetson, and A. M. Turner. A Hubble Space Telescope Study of Extragalactic OB Associations. *Astrophysical Journal*, 116:119–130, July 1998.

[33] A. N. Cox. *Allen's astrophysical quantities*. 2000.

[34] P. Kaaret, M. J. Ward, and A. Zezas. High-resolution imaging of the HeII λ4686 emission line nebula associated with the ultraluminous X-ray source in Holmberg II. *Monthly Notices of the Royal Astronomical Society*, 351:L83–L88, July 2004.

[35] F. Grisé, P. Kaaret, M. W. Pakull, and C. Motch. Optical Properties of the Ultraluminous X-Ray Source Holmberg IX X-1 and Its Stellar Environment. *The Astrophysical Journal*, 734:23, June 2011.

[36] H. Feng and P. Kaaret. Optical Counterpart of the Ultraluminous X-Ray Source IC 342 X-1. *The Astrophysical Journal*, 675:1067–1075, March 2008.

[37] J.-F. Liu. No Periodicity Revealed for an "Eclipsing" Ultraluminous Supersoft X-Ray Source in M81. *The Astrophysical Journal Supplement Series*, 177:181–188, July 2008.

[38] J.-F. Liu, J. N. Bregman, and P. Seitzer. The Optical Counterpart of an Ultraluminous X-Ray Object in M81. *The Astrophysical Journal Letters*, 580:L31–L34, November 2002.

[39] K. D. Kuntz, R. A. Gruendl, Y.-H. Chu, C.-H. R. Chen, M. Still, K. Mukai, and R. F. Mushotzky. The Optical Counterpart of M101 ULX-1. *The Astrophysical Journal Letters*, 620:L31–L34, February 2005.

[40] C. J. Ramsey, R. M. Williams, R. A. Gruendl, C.-H. R. Chen, Y.-H. Chu, and Q. D. Wang. An Optical Study of Stellar and Interstellar Environments of Seven Luminous and Ultraluminous X-Ray Sources. *The Astrophysical Journal*, 641:241–251, April 2006.

[41] J.-F. Liu, J. N. Bregman, and P. Seitzer. The Optical Counterpart of an Ultraluminous X-Ray Source in NGC 5204. *The Astrophysical Journal*, 602:249–256, February 2004.

[42] C. C. Lang, P. Kaaret, S. Corbel, and A. Mercer. A Radio Nebula Surrounding the Ultraluminous X-Ray Source in NGC 5408. *The Astrophysical Journal*, 666:79–85, September 2007.

[43] P. Kaaret, H. Feng, D. S. Wong, and L. Tao. Direct Detection of an Ultraluminous Ultraviolet Source. *The Astrophysical Journal Letters*, 714:L167–L170, May 2010.

[44] L. Tao, H. Feng, F. Grisé, and P. Kaaret. Compact Optical Counterparts of Ultraluminous X-Ray Sources. *The Astrophysical Journal*, 737:81, August 2011.

[45] C. Motch, M. W. Pakull, F. Grisé, and R. Soria. The supergiant optical counterpart of ULX P13 in NGC 7793. *Astronomische Nachrichten*, 332:367, May 2011.

[46] N. Langer and A. Maeder. The problem of the blue-to-red supergiant ratio in galaxies. *Astronomy and Astrophysics*, 295:685, March 1995.